Comparison of DEM Results and Lagrangian Experimental Data for the Flow and Mixing of Granules in a Rotating Drum

Ebrahim Alizadeh, Francois Bertrand, and Jamal Chaouki
Dept. of Chemical Engineering, École Polytechnique de Montréal, C.P. 6079 succ. Centre-Ville, Montréal, QC H3C 3A7, Canada

DOI 10.1002/aic.14259
Published online November 15, 2013 in Wiley Online Library (wileyonlinelibrary.com)

This work assesses the accuracy of the discrete element method (DEM) for the simulation of solids mixing using non-intrusive Lagrangian radioactive particle tracking data, and explains why it may provide physically sound results even when non-real particle properties are used. The simulation results concern the size segregation of polydisperse granules in a rotating drum operated in rolling mode. Given that the DEM is sensitive to simulation parameters, the granule properties were measured experimentally or extracted from the literature. Several flow phenomena are investigated numerically and experimentally, including the particle residence time, the radial segregation, and the radial variation of the axial dispersion coefficient. An analysis of the DEM model is then presented, with an emphasis on the Young's modulus and friction coefficients. Finally, dimensionless motion equations and corresponding dimensionless numbers are derived to investigate the effect of simulation parameters on particle dynamics. © 2013 American Institute of Chemical Engineers *AIChE J*, 60: 60–75, 2014

Keywords: discrete element method, radioactive particle tracking, Lagrangian method, solids mixing, size segregation, rotating drum, physical properties

Introduction

Granular materials are widely used in processes found for instance in the mineral, ceramic, cement, metallurgical, food, and pharmaceutical industries. A common device for handling granular materials is the rotating drum utilized for various purposes. Regardless of the geometrical simplicity of such drums, the flow of material within these devices is quite complex. Depending on the range of Froude numbers $\mathrm{Fr} = \left(\frac{\omega^2 R_D}{g}\right)$, the fill levels and the frictions coefficients between the particles and the drum, different types of transverse bed motions can be observed,[1] where ω, R_D, and g stand for the rotational speed, the drum radius, and the gravitational acceleration. The most critical regime for the purpose of mixing is rolling.[2] This type of motion is characterized by a uniform flow of particles on a free flowing layer (active layer) located at the top of the bed, while the particles in the large underneath layer (passive layer) are transported upwards by the solid body motion of the drum wall. It is well-known that in rolling mode, the bed has a flat surface inclined at a dynamic repose angle.[3–5]

Understanding and controlling the granular flow and mixing behavior in a rotating drum (as well as in other tumbling blenders) are of paramount importance for many industries. Inadequate mixing may result in rejection of the finished product due to poor quality. Unfortunately, there is insufficient knowledge concerning the mixing of granular materials. Therefore, further understanding of granular flow is required to better grasp the mixing mechanisms as well as to design more efficient installations. In the past 25 years, many attempts have been made to comprehend the flow, handling, and characterization of granular materials. In spite of such efforts, the mixing of granular solids is still not well-understood as fluid mixing, due to the complex dynamic behavior involved.

To determine mixing time or measure blend uniformity, several measurement techniques have been proposed. Light induced fluorescence (LIF), near-infrared reflectance spectroscopy (NIR), and effusivity are some of the techniques that are currently available.[6] Characterizing granular mixing is also possible via physical sampling (e.g., thief sampling), which, however, interferes with the matter and affects the measure itself.[7] To overcome the limitations of physical sampling and to measure granular flow dynamics, several nonintrusive methods have been developed. Unfortunately, the granular media is opaque, thereby limiting most of these measurement techniques (including optical and visual methods) inside the granular assembly. Moreover, the available optical experimental methods are limited to visualizing the granular surface. Among these methods, particle image velocimetry (PIV)[8] and particle tracking velocimetry (PTV)[9] are primarily applied. Magnetic resonance imaging (MRI) is another technique, capable of visualizing the bulk of the granular bed.[10] However, difficulty in obtaining MRI signals from solid samples restricts this method, thereby rendering it generally inapplicable to a wide range of granules.[11] MRI cannot be used to examine the flow of granules in any type

Correspondence concerning this article should be addressed to F. Bertrand at francois.bertrand@polymtl.ca and J. Chaouki at jamal.chaouki@polymtl.ca

or size of geometry since the apparatus must fit within the MRI machine. Its high cost is another issue.

There are two radioactive-based methods, which follow a single-labeled tracer in the granular bed. One is known as positron emission particle tracking (PEPT) and uses positron annihilation. This method was developed by Hawkesworth et al.[12] and applied to the rotating drum a few years later.[13] The other method, the results of which are used in this work, is known as radioactive particle tracking (RPT) and is based on the attenuation of gamma rays in the material. This technique was originally developed by Lin et al.[14] and applied by Larachi et al.[15] It has been used for the rotating drum[5,16] and extended for geometries with irregular moving boundaries, such as the V-blender.[17] The RPT in comparison with the PEPT is less costly, compact, and can be used for larger vessels, whereas PEPT is more efficient for investigating systems with complicated free surfaces.

Apart from efforts to develop nonintrusive techniques, numerical methods have progressed, and both continuum models and particle dynamics simulations have been developed. The first approach is Eulerian, which considers powders as a fluid,[18] and the second approach is Lagrangian, which treats particles in the discrete domain. The latter approach, the discrete element method (DEM), originally proposed by Cundall and Strack,[19] has been applied to investigate granular flow in many applications. This simulation technique is a soft particle method and has proven efficient in providing insight into phenomena occurring in granular beds as well as details about the flow and mixing of granules.

Unresolved questions about granular flow and the ability of DEM to predict these types of flow have generated considerable interest, resulting in extensive research works on the subject in recent years. However, few comparisons with experimental data have been performed to examine the validity of the DEM.[11,20–22] Such studies in the literature are mostly qualitative via visual comparison of flow patterns. For instance, Moakher et al.[23] considered double-cone and V-blenders, and Iwasaki et al.[24] studied a high-speed elliptical rotor-type powder mixer, both groups demonstrating that calculated flow patterns agreed with experimental observations. Although there is a limited number of techniques capable of providing Lagrangian data and mapping the velocity field inside opaque granular systems, studies that quantitatively validate the DEM at the particle scale are limited. Such studies, which are mostly based on PEPT, can be found in Laurent and Cleary[25] and Stewart et al.[26] Despite the importance of previous investigations, comparisons of Lagrangian experimental and DEM-based model continue to be inadequately thorough. Indeed, in many studies, real values of particle properties have not been used for the DEM simulations and neither have they been experimentally measured. Although these parameters demonstrate a high effect on the granular flow, researchers have often adjusted them to obtain results that agree well with experimental observations.

The challenge of this work is to assess the accuracy of a DEM-based model and explain why physically sound results may be obtained even when nonreal particle properties are used. To do so, a detailed and thorough comparison is provided between Lagrangian experimental data of the RPT and numerical results of the DEM. The granular properties were measured experimentally or extracted from the literature. This work is restricted to the simple geometry of a rotating drum and, as a consequence, does not look into geometrical effects on the flow behavior. The granules are glass beads and the drum was operated in rolling mode. Moreover, in this work, a polydisperse mixture with a precise particle-size distribution is considered (four different size particles), whereas in the literature a binary mixture has generally been the subject of study.[27,28] First, details of the phenomena occurring inside the rotating drum are investigated including radial and axial segregation, velocity profiles, residence times of granules, and axial dispersion. Next, to evidence the sensitivity of DEM results to the particle mechanical and physical properties, dimensionless motion equations of particles in normal and tangential directions are derived and analyzed. Finally, effective dimensionless numbers are introduced to explain how the DEM parameters should be chosen.

Methodology

RPT experiments

The RPT technique follows a radioactively marked particle having similar physical and mechanical properties as the inert particles in the bed, to provide a three-dimensional (3-D) position of this tracer with respect to time. The tracers were activated in the Slowpoke nuclear reactor of École Polytechnique de Montréal, and the activity level was initially approximately 2.22 MBq thanks to presence of ^{24}Na. Eight $3'' \times 3''$ NaI scintillation detectors were installed around the drum made of Plexiglas with a 24-cm internal diameter and 36-cm length. The drum was filled up to 35 vol% with soda lime glass beads and its rotational speed was 11.6 RPM.

Experiments and blend characteristics are shown in Table 1. Two sets of RPT experiments were performed. In the first one that comes from our previous work,[5] each case lasted 210 min. Due to the occurrence of segregation in these experiments, the ergodic hypothesis did not hold and the flow of one single tracer could not be used to represent the trajectories of many particles.[29] As a result, segregation was only assessed in a global manner by means of occupancy plots. In the current work, the goal was to look into segregation more deeply by resorting to mixing indices that were developed in our group,[30] as will be further discussed later. Therefore, a second set of experiments was carried out, where each case lasted 2 minutes and was repeated 50 times with a randomly chosen initial position for the corresponding tracer. Further details of the experimental procedure can be found in Alizadeh et al.[5]

DEM simulation

A DEM simulation tracks the position of the particles of a granular system by solving Newton's equation of motion on each of them. In this study, the total force acting on each particle includes gravity as well as a contact force term that accounts for the particle/particle and particle/wall interactions. Due to the particle size in the order of a few millimeters (3–6 mm), the colloidal forces can be neglected. The drag force, F_D, can be obtained through

$$F_D = \frac{1}{2} c_D \rho_f v_{pf}^2 A_D, \tag{1}$$

where C_D is the drag coefficient, ρ_f the density of the fluid (air), v_{pf} the particle-fluid relative velocity, and A_D the cross-sectional area of the particle. Due to the rather large

Table 1. RPT Experiments and Blend Characteristics

Case	Blend Type	Rotational Speed Ω (RPM)	Tracer Size (mm)	Experiment Duration (Min)	
				First Set Alizadeh et al.[5]	Second Set (New Data)
A	Polydisperse (3mm (15 vol %), 4mm (35 vol %), 5mm (35 vol %), 6mm (15 vol %))	11.6	3	210	2 (×50)
B		11.6	4	210	2 (×50)
C		11.6	5	210	2 (×50)
D		11.6	6	210	2 (×50)

particle size, the low density of air and the small relative particle velocity, the drag forces can also be neglected. A model is required to estimate the contact force term. In this work, the contact force acting on particle i when it is colliding with another particle j is decomposed in normal (head-on) and tangential (shear) components, and the following nonlinear viscoelastic model is used

$$\begin{aligned} F^n &= F^n_{\text{el}} + F^n_{\text{dis}} \\ &= k_n \xi_n^{\alpha} + S_n \xi_n^{\beta} \dot{\xi}_n, \end{aligned} \tag{2}$$

$$\begin{aligned} F^t &= F^t_{\text{el}} + F^t_{\text{dis}} \\ &= k_t f_1(\xi_t) + S_t f_2(\xi_t) \dot{\xi}_t. \end{aligned} \tag{3}$$

The first and second terms in this model correspond to repulsion and dissipation forces, respectively. ξ_n and $\xi_t$are the normal and tangential components of the overlap between contacting particles i and j, kn, and kt stiffness coefficients, S_n and S_t damping coefficients, and α and β nonlinear constants that depend on the model. A review of the normal and tangential contact force models can be found in Kruggel-Emden et al.[31,32] and Alizadeh et al.[33] In this study, the contact force model is similar to those of Zhou et al.[34] and Baxter et al.[35] In particular, $\alpha=\frac{3}{2}$ and $\beta=\frac{1}{4}$ are set to evaluate the normal elastic force with the Hertz theory and the normal dissipative term with a model proposed by Tsuji et al.[36] The stiffness (k_n and k_t) and damping coefficients $\left(S_n=-s_n\sqrt{6m^*E^*\sqrt{R^*}} \text{ and } S_t=-s_t\sqrt{\frac{6\mu_s m^*|F^n_{el}|}{\xi_{t,m}}}\right)$ are functions of the Young's modulus E, Poisson's ratio v, damping constants (s_n and s_t) as well as static and dynamic friction coefficients (μ_s and μ)

$$F^n_{\text{el}} = -\frac{4}{3}E^*\sqrt{R^*}\xi_n^{\frac{3}{2}}, \tag{4}$$

$$F^n_{\text{dis}} = -s_n\left(6m^*E^*\sqrt{R^*}\right)^{\frac{1}{2}}\xi_n^{\frac{1}{4}}\dot{\xi}_n, \tag{5}$$

$$F^t_{\text{el}} = -\mu_s|F^n_{el}|f_1(\xi_t), \tag{6}$$

$$F^t_{\text{dis}} = -s_t\left(6\mu_s m^*|F^n_{el}|\frac{f_2(\xi_t)}{\xi_{t,m}}\right)^{1/2}\dot{\xi}_t, \tag{7}$$

where R^* is the reduced radius $\left(\frac{1}{R^*}=\frac{1}{R_i}+\frac{1}{R_j}\right)$, E^* is the reduced Young's modulus $\left(\frac{1}{E^*}=\frac{1-v_i^2}{E_i}+\frac{1-v_j^2}{E_j}\right)$, m^* is the reduced mass of particles i and j $\left(\frac{1}{m^*}=\frac{1}{m_i}+\frac{1}{m_j}\right)$, $\xi_{t,m}=\mu\frac{(2-v)}{2(1-v)}\xi_n$ is the maximum tangential deformation. $f_1(\xi_t)$ and $f_2(\xi_t)$ in Eqs. 6 and 7 are defined as $f_1(\xi_t)=1-\left(1-\frac{\min(\xi_t,\xi_{t,m})}{\xi_{t,m}}\right)^{3/2}$ and $f_2(\xi_t)=\sqrt{1-|\xi_t|/\xi_{t,m}}$. The tangential force is bounded by $\left(\mu|F^n_{el}|\right)$, following the Coulomb law of friction.

Choosing a proper time step for a DEM simulation is generally a trade-off between the CPU time, the numerical error, and the stability of the integration scheme. The time step should be smaller than the characteristic time τ_c, which corresponds to a typical contact time between two colliding particles[37]

$$\tau_c = \frac{\pi\overline{R}}{\varepsilon}\sqrt{\frac{\rho}{G}}, \tag{8}$$

where ρ is the particle density, $\overline{R}$ is the average particle radius, and $G=\frac{E}{2(1+v)}$ is the particle shear modulus. ε can be obtained from[38]

$$\left(2-\varepsilon^2\right)^4 = 16\left(1-\varepsilon^2\right)\left[1-\varepsilon^2\frac{1-2v}{2(1-v)}\right], \tag{9}$$

which can be approximated by[39]

$$\varepsilon = 0.8766 + 0.163v. \tag{10}$$

In systems with smaller characteristic times (small particles, high stiffness or high velocities), a DEM simulation can maintain its stability if a small enough time step is used. In this study, this time step corresponds to 1.2 μs, which explains why corresponding DEM simulations are CPU-intensive. The detailed particle information (position and velocity) was stored at 0.033 s intervals. To reduce the CPU time, the computational domain was decomposed into subdomains and the code was run in parallel through the MPI communication library using 32 cores of parallel clusters of Compute Canada.

For the polydisperse system of this work, the simulation comprised 83,000 particles, the size of which complied with the distributions used for the RPT experiments (see Table 1). Each simulation was done using our own DEM code and an initially homogenous mixed state, for a total simulated time of 120 s. The total computation time of each simulation was 35 days.

Results and Discussion

This section discusses the DEM parameters and how they were measured. Next, the DEM simulation results are compared to the experimental RPT data. To this end, results concerning the velocity profiles, the residence times of granules, the segregation, and the axial dispersion of granules are analyzed. Finally, an analysis of the DEM is performed to demonstrate the effects of granules properties on the results. Note that the results of the first set of RPT experiments are applied unless otherwise mentioned.

DEM parameters

Here, the focus is on the properties of granules used for the DEM simulations. The measured properties of the soda

Table 2. DEM-Based Model Parameters (Measured and Applied)

Properties	Measured	DEM Simulation	Measurement Technique or Reference
Particle/Particle			
Density $\rho(g/cm^3)$	2.5	2.5	Bolz and Tuve[40]
Young's modulus E (MPa)	68,900	200	Bolz and Tuve[40]
Poisson's ratio v	0.24	0.24	Bolz and Tuve[40]
Normal damping constant s_n	0.0075	0.0075	Foerster et al.[41]
Tangential damping constant s_t	–	0.02	Same as particle/wall
Dynamic friction coefficient μ	0.092 ± 0.006	0.06	Foerster et al.[41]
Static friction coefficient μ_s	0.16–0.29	0.16	Amstock[42]
Particle/Wall			
Normal damping constant $s_{n,w}$	0.06–0.075	0.065	High-speed camera
Tangential damping constant $s_{t,w}$	0.02	0.02	High-speed camera
Dynamic friction coefficient μ_w	0.083 ± 0.012 (fresh glass) 0.135 ± 0.009 (scratched glass)	0.35	High-speed camera + force balance
Static friction coefficient $\mu_{w,s}$	0.179 ± 0.016 (fresh glass) 0.208 ± 0.026 (scratched glass)	0.45	Inclined plate + force balance
Rolling friction coefficient μ_r	–	2.5×10^{-5}	Zhou et al.[43]

The particle/wall impact properties were measured with the techniques mentioned and the particle/particle impact properties were extracted from the literature.

lime glass beads in the case of particle/particle and particle/wall impacts are presented in the second column of Table 2. Some properties were measured experimentally, whereas others were extracted from the literature. The third column of the table illustrates the parameters used for a DEM simulation to obtain results that best agree with the RPT experimental data. As can be seen, real values of the glass beads properties were applied except for the Young's modulus and the friction coefficients. Explanations are given below as more details are given on the properties of the glass beads and how they were measured.

Physical and Mechanical Properties. The particles used in this work are commercially available soda-lime glass beads from Fisher Scientific with a density of 2.5 g/cm^3, a Young's modulus of 6.8×10^{10} Pa, and Poisson's ratio of 0.24.[40] Such a high value of the Young's modulus indicates that the glass beads are stiff. A collision between two such granules has a short contact duration time (see Eq. 8) and, consequently, DEM simulations involving this type of solid particles require small time steps and large computational times. To overcome this limitation, the Young's modulus of such granules or its equivalent (stiffness coefficient in Eq. 2) is generally reduced to increase the duration of a collision and allow for a bigger time step.[31] This is indeed common in the literature, and the fourth column of Table 3 indicates the typical values of the Young's modulus that have been applied in the cited investigations. Note that some recent investigations have considered real values of the Young's modulus.[57–62] However, these studies have pertained to very soft material (e.g., microcrystalline cellulose or agricultural seeds) or very small numbers of particles, sometimes in 2-D systems. Therefore, in this study, the Young's modulus was set at 200 MPa, which is relatively high in comparison with the values used in the literature (Table 3). For such a value of the Young's modulus, a time step of 1.2 μs was chosen, which is smaller than the characteristic time τ_c(see Eq. 8) and enabled the simulations to be run on the parallel computers of Compute Canada. Note that the effect of the Young's modulus on the simulation results will be further discussed in this section, where an analysis of the DEM results with respect to the granule physical properties is presented.

Coefficients of Restitution. Given that particles collide with the blender wall and other particles, characterizing particle/particle and particle/wall impacts is essential. The velocity of the particles after each contact can be found via the coefficient of restitution (CoR), which is the ratio of the particle velocities after and before a collision in both normal and tangential directions.

To obtain the normal CoR (CoR_n) of glass beads against a solid wall, their impact during free fall under gravity was considered. The impact was perpendicular and against a horizontal Plexiglas plate (same material as that used for the drum). Before the impact, the particle was held at an appropriate height by a vacuum nozzle. The particle was then released, without any spin or initial velocity. A high-speed camera was used to record the details of the impact at a rate of 200 frames per second. The initial height of the particles was varied (0.10–0.23 m) to cover a wide range of impacting velocities (1.4–2.1 m/s). The impact velocity was calculated using the conservation of mechanical energy. More details about the experimental procedure can be found in Alizadeh et al.[33] The measured normal CoR was 0.82 ± 0.02 for this velocity range. Next, particle/particle normal CoR values were obtained directly from the literature: 0.97 ± 0.01 for a velocity range of 0.64–1.2 m/s.[41] Damping constants $s_n = 0.0075$ and $s_{n,w} = 0.065$ were then backed out from DEM simulations involving one single contact in the case of particle/particle and particle/wall collisions, respectively.

The same technique as for the normal CoR was applied to measure the tangential CoR (CoR_t) on a plate. The initial height was fixed at $\sim$5 cm, leading to an impact velocity of $\sim$1 m/s. The impact angle was varied from 5° to 55° by adjusting the position of the plate. It was observed that the tangential CoR increases when the impact angle increases, which is in agreement with data reported in the literature.[63] DEM simulations revealed that $s_{t,w} = 0.02$ fits best these experimental data. Moreover, it was found that a small variation in damping constant s_t has no significant impact on the dynamics of granules, and only minor effects on the mixing behavior inside the drum. This is mainly due to the fact that the glass beads have a high CoR so that the dissipative force is relatively small in the motion equation. Therefore, no experiment was performed to measure its value for particle/particle impact and it was chosen to be the same as $s_{t,w}$.

Friction Coefficients. To measure the particle/wall static friction coefficient, three particles were glued onto a plate and then put in contact with a fresh Plexiglas sheet. This

Table 3. Values of the Young's Modulus (E) and Friction Coefficients Used in DEM Simulations from the Literature that have Led to Acceptable Results

	Real Particles Properties		Applied DEM Parameters		
Real Particles	E (GPa)	μ	E (MPA)	μ	References
Glass beads	68.9	0.092	4.87	0.5	Bouffard et al.[44]
Pure numerical simulation	–	–	0.3	0.3, 0.6	Balevicius et al.[45]
Avicel PH101	7.4–10.3[46]	0.15–0.4[47]	2	0.375–0.5	Lemieux et al.[21,48]
Glass beads	68.9	0.092	–	0.3, 0.5	Taberlet et al.[22,49]
and steel beads	193	0.23[50]			
Glass beads	68.9	0.092	10–200	0.3, 0.5	Yang et al.[51,52]
Wheat grains	0.3–20[53]	0.35–0.6[54]	–	0.5	Schutyser et al.[55]
and green peas	–	–			
Glass beads	68.9	0.092	1–2.16	μ=0.4, μ_w=0.7	Zhou et al.[34,43]
Glass beads	68.9	0.092	2.16	0.3, 0.5	Stewart et al.[26]
Polypropylene	1.34	0.1–0.3	–	0.3	Kaneko et al.[56]
Vulcanite	–	–	–	μ=0.2, μ_w=0.4	Dury et al.[4]

When E is not given, the stiffness constant (k_n in Eq. 2) has been reported directly in the corresponding article.

Plexiglas sheet was gradually inclined until the particles started to slide.[64] By means of a force balance, the static friction coefficient was calculated to be the tangent of the angle θ_s at which these particles started to slide $\left(\mu_{w,s}=tan(\theta_s)\right)$. To obtain the dynamic friction coefficient, glued particles were allowed to slide on the inclined Plexiglas sheet $(\theta > \theta_s)$ from a zero initial velocity. The distance and time duration during an experiment were recorded by a high-speed camera. Newton's second law of motion then yielded a value for this coefficient. The values of the dynamic and static friction coefficients of soda-lime glass beads on a fresh Plexiglas sheet obtained with this technique are 0.083 ± 0.012 and 0.179 ± 0.016, respectively. The drum wall used for the experiments is made of Plexiglas but is not as smooth as a fresh Plexiglas sheet. Therefore, dynamic and static friction coefficients of soda-lime glass beads on a scratched Plexiglas were also measured using the same technique. The values obtained are 0.135 ± 0.009 and 0.208 ± 0.026, respectively. The dynamic and static friction coefficients of particle/particle collision were obtained from the literature, 0.092 ± 0.006 and 0.16–0.29, respectively.[41,42] Note that it is common in the literature to use identical values of the dynamic and static friction coefficients, for both particle/particle and particle/wall impacts, which in most cases are above 0.3 (see the fifth column of Table 3). In this study, different values of friction coefficients were chosen for the DEM simulations: μ= 0.06, μ_s= 0.16, μ_w= 0.35, and $\mu_{w,s} = 0.45$. These values are in fact different from those measured, to compensate for the effect of using a smaller value of the Young's modulus. They were set in a way to have nonslipping dynamics for the granules close to the wall region of the drum and match the simulated dynamic repose angle and that obtained by RPT. This will be further discussed in the section on the analysis of the DEM-based model.

Velocity profiles and active layer thickness

The investigation of the particle dynamics inside the drum leads to a better understanding of mixing and segregation mechanisms, and ultimately helps design more efficient unit operations. Both the RPT method and DEM-based model were used to obtain particle velocity profiles. In the DEM simulations, the particle velocities were stored at each time interval (0.033 s), whereas in RPT, they were derived from the tracer displacement. Figures 1a, b show the time-averaged velocity profiles in the transverse plane of the drum, respectively, obtained by DEM and RPT, as well as their subtraction in Figure 1c. As can be seen, there is good agreement between these DEM and RPT results with some differences near the free surface. Variations in streamwise velocity u_x (x-direction) along a line perpendicular to the bed surface at $x = 0$ is shown in Figure 2. The x and y axes are shown in Figure 1. A linear fit describes the flow of particles in the active layer (solid line), whereas a straight line from the drum center (dashed line) goes through the data points in the passive layer, complying with the solid body rotation, $u_x = -\omega y$, expected therein. Similar results (not presented) were obtained for other x-positions. Here again, a good agreement between the RPT data and the DEM results was observed.

The depth at which the particles stop moving as a solid body and start free flowing is the boundary between the active and passive layers (δ in Figure 2). According to the RPT and DEM results, the maximum depth of the active layer $\left(\delta_o=\delta|_{x=0}\right)$ was obtained at 4.2 cm, which is 48% into the material bed. Many studies dealing with the active layer thickness exist,[65–68] although the definition of the thickness varies. It can also be defined as the point where the particles change direction ($u_x = 0$) along the x axis, as defined by δ' in Figure 2. For both our experimental and simulation results, $\left(\delta'_o=\delta'|_{x=0}\right)$ was measured at 2.9 cm, which is 33% into the material bed.

The particle velocity profile at the free surface is plotted as a function of the normalized x position in Figure 3a. The profiles have been normalized with respect to the velocity at midchord position $\left(u_{x,\max}=u_x|_{(x=0,y=-H)}\right)$. The solid line is a parabolic functions, $u_x/u_{x,\max} = 1-\left(\frac{x}{L}\right)^2$, where L is the half-length of the free surface. Similar results were previously shown by Ding et al.[69] and Alizadeh et al.[5]

Figure 3b shows the variation in surface velocity across the axial direction of the drum, as obtained by the DEM and the RPT. In both cases, the velocity vectors near the end walls ($|z| = +0.18$ m) are different from those in the middle of the drum ($z = 0$), with a small axial component. This has also been reported in the literature[70] and can be attributed to the end-wall friction, which projects the particles above the free surface and away from the end-wall in the axial

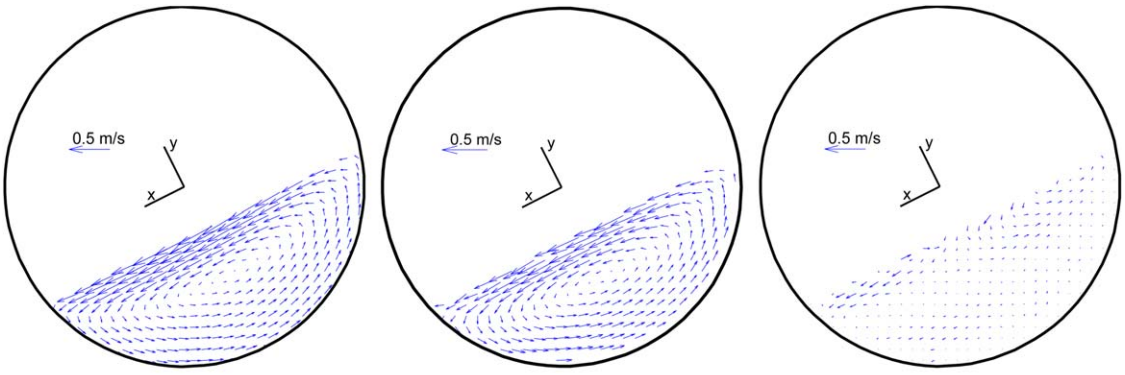

(a) DEM (b) RPT (c) DEM vs. RPT

Figure 1. Typical time-averaged velocity vectors obtained by (a) the DEM simulations and (b) RPT experiments, (c) differences in the velocity vectors displayed in (a) and (b).

[Color figure can be viewed in the online issue, which is available at wileyonlinelibrary.com.]

direction. The axial flow of the particles downstream toward the wall may then be explained by the conservation of mass.

End-wall friction also affects the dynamic repose angle of the granules, which is higher in regions near the end walls (34°) than in the middle of the cylinder (27°). The former was predicted by the DEM simulations and the latter was obtained both from RPT data and DEM results. The influence of these walls seems to be short-ranged, and the dynamic repose angle drops rapidly within a few centimeters to its value in the middle of the drum. Note that this phenomenon was observed in the DEM simulations only, due to the use of particle/wall friction parameters larger than the real ones (see Table 2). Our RPT results did not show significant differences along the drum. The increase of the repose angle near the end walls was also reported by Dury et al.[4] who measured the variations of the repose angle along the axial direction by means of DEM simulation. To obtain such results, these authors adjusted the particle/wall friction coefficients, the values of which are presented in Table 3.

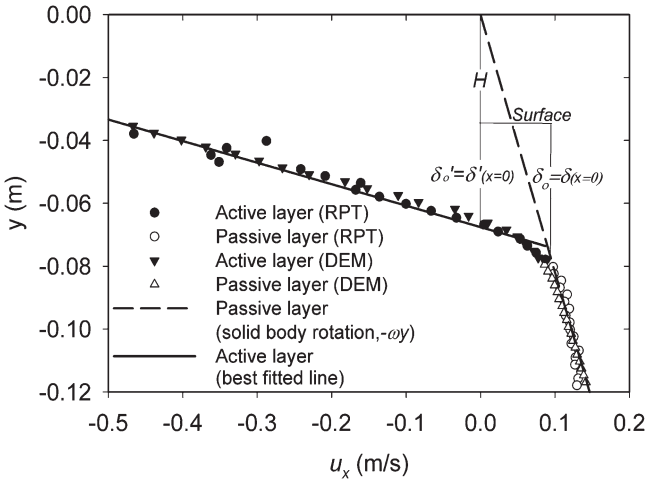

Figure 2. Streamwise velocity profile at $x = 0$ as seen from the drum end wall.

The vertical axis represents the distance from the center of the drum, and the horizontal axis represents the streamwise velocity. H is the distance from the center of the drum to the free surface of material, $\delta_o$is the distance from the free surface to the depth at which the solid body rotation of the bed of particles stops, and δ'_o is the distance from the free surface to the depth at which these particles change direction along the x axis.

Residence time

In the rotating drum, the transverse motion of the particles is the primary factor controlling the renewal of the material at the exposed bed surface. The residence times in the active and passive layers have an impact on the efficiency of many processes such as pan coating where a solution (e.g., binder) is top-sprayed on the surface of the bed of particles.[5] It was shown in this earlier work, through RPT data, that the residence time in the active layer can be evaluated through the following expression for notations (see Figure 4a)

$$t_{\mathrm{act}} = t_{b\to b'} = \frac{3.87\delta_{\mathrm{o}}'}{\omega L}, \tag{11}$$

Following along the lines of Dube et al.,[71] the residence time in the passive layer can be obtained according to the following equation if it is assumed that $t_{a\to b}=t_{b'\to a'}$

$$t_{\mathrm{pas}} = \frac{1}{\omega}\gamma + 2t_{a\to b}, \tag{12}$$

where γ is the angle of the streamline. Neglecting the small differences between x_a and x_b ($x_a \simeq x_b$) gives

$$t_{a\to b} = \int_a^b \frac{\mathrm{d}y}{u_y}, \tag{13}$$

where u_y is the transverse velocity[72]

$$u_y = -\frac{\omega x(y+H)}{\delta(x)}. \tag{14}$$

Equation 13 can be approximated by

$$t_{a\to b} = \frac{y_b - y_a}{\overline{u}_y} = \frac{\delta(x) - \delta'(x)}{\overline{u}_y}, \tag{15}$$

where

$$\overline{u}_y = \frac{1}{y_b - y_a}\int_a^b u_y dy = -\frac{\omega x(y_b + y_a + 2H)}{2\delta(x)}. \tag{16}$$

From $\delta(x) = -(y_a + H)$ and $\delta'(x) = -(y_b + H)$, it follows that

$$\overline{u}_y = \frac{\omega x\left[\delta'(x) + \delta(x)\right]}{2\delta(x)}, \tag{17}$$

where the values of $\delta(x)$ and $\delta'(x)$ can be estimated by assuming that the boundary between the active and the passive layers is parabolic

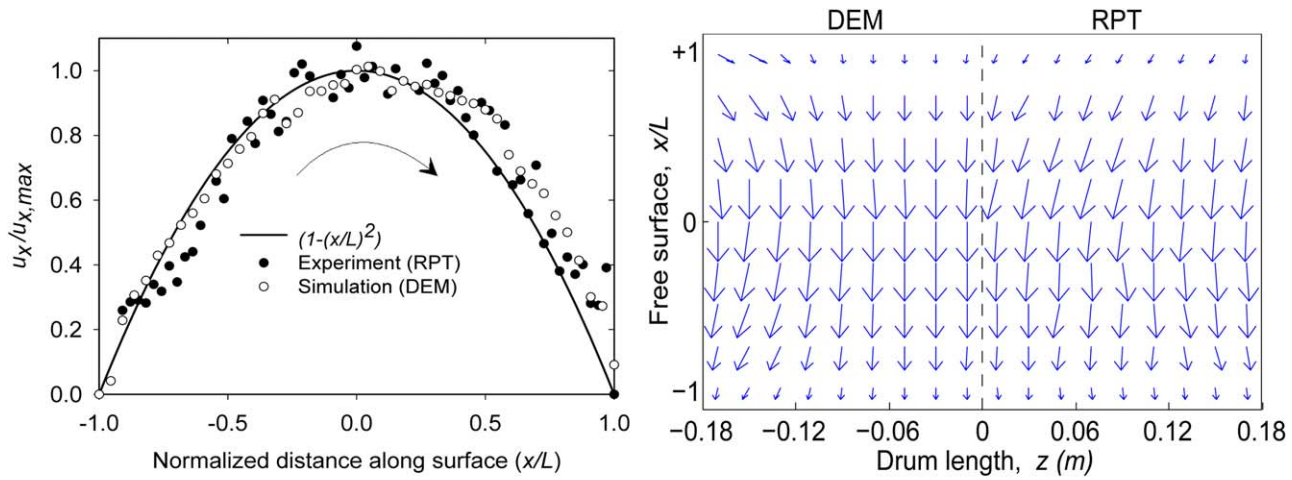

(a) (b)

Figure 3. Surface velocity profiles: (a) normalized streamwise velocity vs. the dimensionless distance along the surface, (b) velocity vectors at the free surface along the drum length, where the DEM (resp. RPT) results are used for the left (resp. right) side of the drum.

[Color figure can be viewed in the online issue, which is available at wileyonlinelibrary.com.]

$$\delta(x)=\delta_o\left(1-\frac{x^2}{L^2}\right), \tag{18}$$

$$\delta'(x)=\delta'_o\left(1-\frac{x^2}{L^2}\right). \tag{19}$$

Substituting Eq. 15 into Eq. 12 and using Eq. 17 for $\overline{u}_y$ yield

$$t_{pas}=\frac{1}{\omega}\gamma+4\frac{\left[\delta(x)-\delta'(x)\right]\delta(x)}{\omega x\left[\delta(x)+\delta'(x)\right]}, \tag{20}$$

where x can be readily obtained from

$$\tan\frac{\gamma}{2}=\frac{x}{\delta(x)+H}=\frac{x}{\delta_o\left(1-\frac{x^2}{L^2}\right)+H}. \tag{21}$$

The variation of the residence time in the passive layer vs. the streamline angle (γ) can then be obtained through these steps:

- For each γ, the x–position is obtained from Eq. 21;
- $\delta(x)$ and $\delta'(x)$ are calculated from Eqs. 18 and 19;
- t_{pas} is obtained from Eq. 20.

The residence times in the active and passive layers vs. the angle of the streamlines is provided in Figure 4b. First, it can be seen that the RPT results validates the DEM simulation results. In particular, the residence time in the active

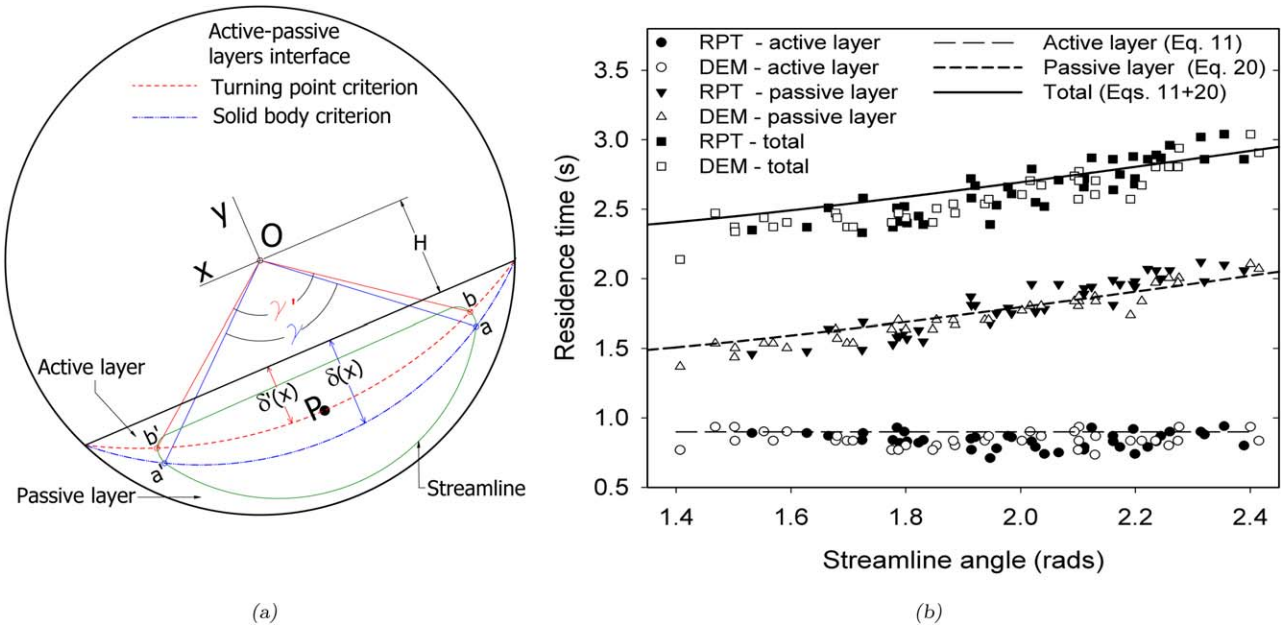

(a) (b)

Figure 4. (a) A streamline making a full rotation in the active and passive layers; (b) variations of the residence times in active and passive layers when the angle of the streamline increases.

[Color figure can be viewed in the online issue, which is available at wileyonlinelibrary.com.]

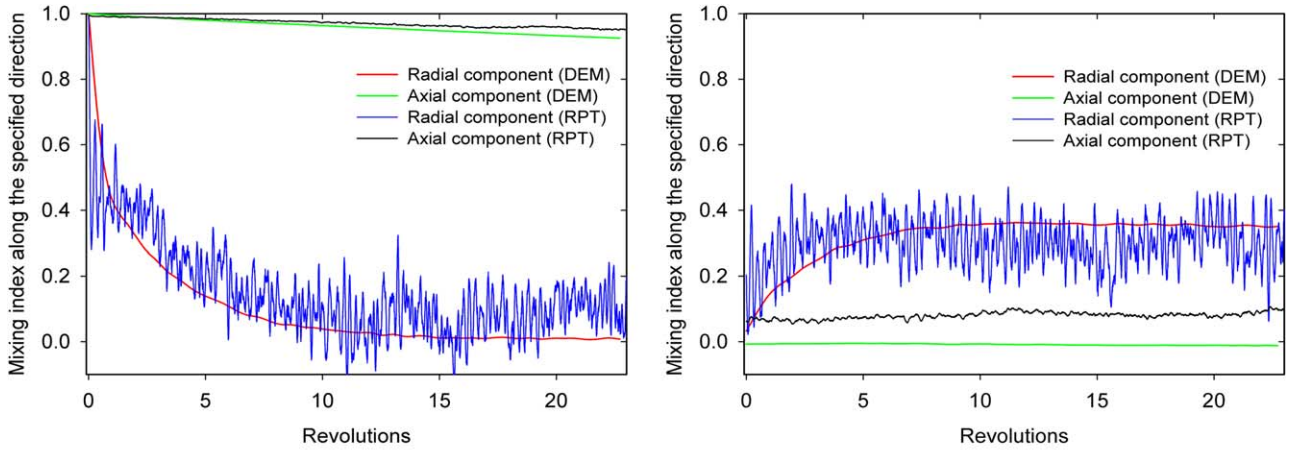

Figure 5. Evolution of the (a) weak sense and (b) strong sense mixing indices along the radial and axial directions.

[Color figure can be viewed in the online issue, which is available at wileyonlinelibrary.com.]

layer is constant when the angle of the streamlines increases. These results are in agreement with the short-dashed line (Eq. 20) in the passive layer, the long-dashed line (Eq. 11) in the active layer and the solid line (total residence time from the sum of Eqs. 11 and 20).

Mixing and segregation in the rotating drum

Lacey[73] demonstrated the usefulness of many methods to assess the state of a mixture. A well-known one for solids mixing is the relative standard deviation (RSD) that measures the standard deviation in composition of a set of samples taken at a certain stage of the mixing operation. Recently, Doucet et al.[30] proposed a new mixing index to bridge the global mixing properties and local viewpoint of chaotic theory, with applications to granular and fluid flow systems. The index is based on the Lagrangian trajectory of particles obtained either numerically through computer simulation or experimentally by means of nonintrusive methods (such as PEPT and RPT). This index has been applied to assess the quality of mixing in pharmaceutical equipment.[44,74] Two different indices were in fact defined by Doucet et al.,[30] which characterize the concept of mixing in the weak and strong senses.

Mixing in the weak sense considers the correlation between the current and initial positions of the particles without respect to their properties, such as size or density. More precisely, given a probability measure Λ with $l^t(i)\left(x_i^t, y_i^t, z_i^t\right)$the position of particle i at time t, a system is said to be mixed in the weak sense if

$$\Lambda\left\{l^t(i)|l^0(i)\right\}=\Lambda\{l^t(i)\}, i=1,2,\ldots,N. \tag{22}$$

In such a case, the position of the particles at time t is not correlated to their initial position. This implies that the particles distribute themselves uniformly in the blender and the corresponding index levels off to zero with respect to time. The development of this mixing index, denoted by $\eta_{ws} \in [0,1]$, is based on principal component analysis and the construction of a correlation matrix that brings into play particle positions $l^t(i)$ and $l^0(i)$. It takes on a value of 0 when the system is perfectly mixed and 1 when it is fully segregated.

Weak sense mixing fails to capture the occurrence of segregation with respect to the particle properties. For this reason, a more strict definition of mixing was introduced, which considers properties of the material and is called mixing in the strong sense. Given a probability measure Λ and $p=\{p_1, p_2 \ldots, p_M\}$a set of particle properties, a system is said to be mixed in the strong sense if

$$\Lambda\left\{l^t(i)|l^0(i), p_1(i), p_2(i), \ldots, p_M(i)\right\}=\Lambda\{l^t(i)\}, i=1,2,\ldots,N. \tag{23}$$

This condition implies that the position of the particles at time t is not correlated to their initial position and other given properties. The corresponding strong sense mixing index then levels off to zero with respect to time. Note that, from these definitions, a system that is mixed in the strong sense is also mixed in the weak sense. Note that it is also possible to define and use similar indices to investigate the intensity of mixing (or segregation) along specific directions (here the radial and axial directions). More details on these indices can be found in Doucet et al.[30]

DEM simulations and the second set of experiments from Table 1 were used to assess mixing in the rotating drum based on these indices. Figure 5a presents the evolution of the weak sense mixing indices in the radial and axial directions for the polydisperse system. As can be observed, there is an agreement between the RPT data and the simulation results. The radial direction curves decay to zero, whereas the axial direction curves decrease slowly but remain near 1 even after 25 blender revolutions. This clearly indicates that overall mixing is limited by inefficient axial mixing, as has already been shown in the literature.[21]

It should be noted that this system is known to lead to both axial and radial segregation.[75,76] To take into account segregation, the strong sense definition of mixing must be considered. Figure 5b shows that the strong sense mixing index in the radial direction levels off to an asymptotic value of around 0.35. This shows that the polydisperse mixture does not mix well in the radial direction. It can also be seen that the final radial segregation state is reached earlier for the RPT data than for the DEM results. Next, it seems that the index is not able to capture the segregation phenomenon that occurs slightly in the axial direction, as the values of this index remain near 0 (slightly larger for the RPT data) after many drum revolutions. The slightly nonzero value of

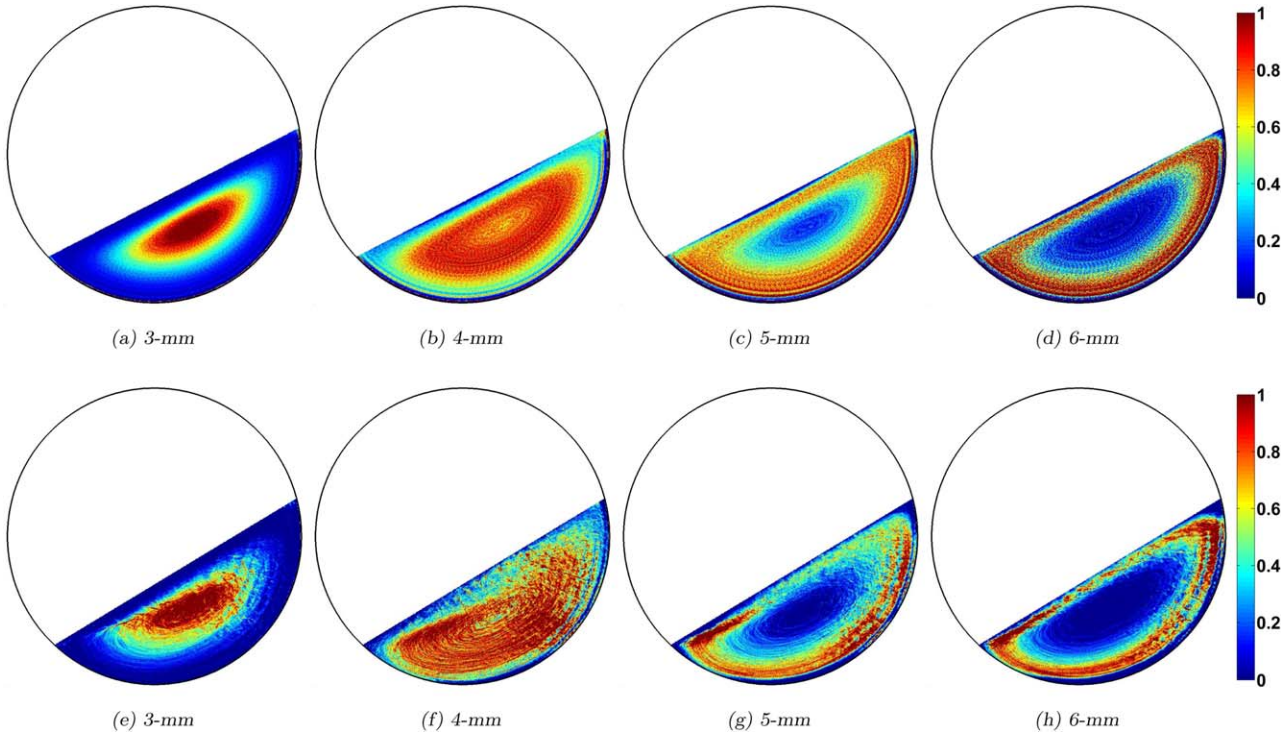

Figure 6. Occupancy plots for the different-sized particles of the polydisperse mixture: (a)–(d) and (e)–(h) were obtained from the DEM and RPT, respectively.

The colors show the probabilities of occurrence of the corresponding particles. The RPT occupancy plots come from Alizadeh et al.[5] [Color figure can be viewed in the online issue, which is available at wileyonlinelibrary.com.]

this index when obtained from the RPT data is due to the nonhomogenous initial axial distribution of the radioactive tracer positions in the 50 experiments, and does not imply axial segregation.

To gain more insight into the radial segregation pattern taking place in the drum, occupancy plots on a transverse plane located midway between both end walls are displayed in Figure 6 for different-sized particles. These plots were obtained by projecting the particle positions onto the transverse plane. As evidenced by both the DEM results and the RPT data, the small 3-mm particles form a core along the material rotation axis and are surrounded by the larger 5-mm and 6-mm particles. The 4-mm particles are present in the entire volume of the drum, although mainly in inner layers.

Occupancy plots do not provide information about the rate at which radial segregation occurs. To do so, the average distance of the particles from the material rotation axis (point P in Figure 4a) can be calculated for each revolution

$$d^t(q)=\frac{\sum_{i=1}^{N_q}|r_i^t-r_p|}{N_q}, q=3,4,5,6, \tag{24}$$

where $d^t(q)$ is the average distance of the particles of size q at time t with respect to point P at radial position r_p, r_i^t the radial position of the ith particle of size q at time t, and N_q the number of particles of size q. This quantity was calculated for both the DEM results and second set of RPT data. Figure 7a shows the time variation of $d^t(q)$, whereas Figure 7b shows its variation along the drum length for $t=120$ s (DEM results only). The following remarks can be made:

1. In Figure 7a, the agreement between the DEM results and RPT data is good, all the more so after 20 revolutions. However, as is shown in Figure 5b, the rate at which radial segregation develops is different in these two cases. In Figure 7a, radial segregation is complete in 5 and 7 revolutions with RPT and DEM, respectively;
2. All curves start approximately from the same point in Figure 7a, confirming that the particles were initially mixed;
3. In Figure 7a, the curves corresponding to the 3-mm and 4-mm particles exhibit a decreasing behavior, whereas they increase in the case of the 5-mm and 6-mm particles. This means that the large (resp. small) particles migrate to outer (resp. inner) layers of the material bed. One would then expect a constant behavior for a particle size of 4.5-mm and, therefore, no radial segregation in such a case. This information could be used to adjust the particle size distribution in a mixture to preclude radial segregation for a selected species;
4. Figure 7b reveals that $d^t(q)$ slightly varies along the axial direction of the drum. There seems to be less segregation in regions close to the end walls than in the middle of the drum. In particular, this shows that characterizing granular flow and mixing in the transverse plane of the drum with techniques that can only visualize the material surface from the end walls (e.g., PIV) is limited. Alternative methods such as RPT are preferable to capture the particle motion inside the rotating drum.

Figure 8 shows the evolution of the axial segregation as predicted by the DEM for the polydisperse mixture. To obtain such plots, the drum was divided into thin cylindrical discs perpendicular to the rotation axis, and the time variation in concentration of each species in every disk was

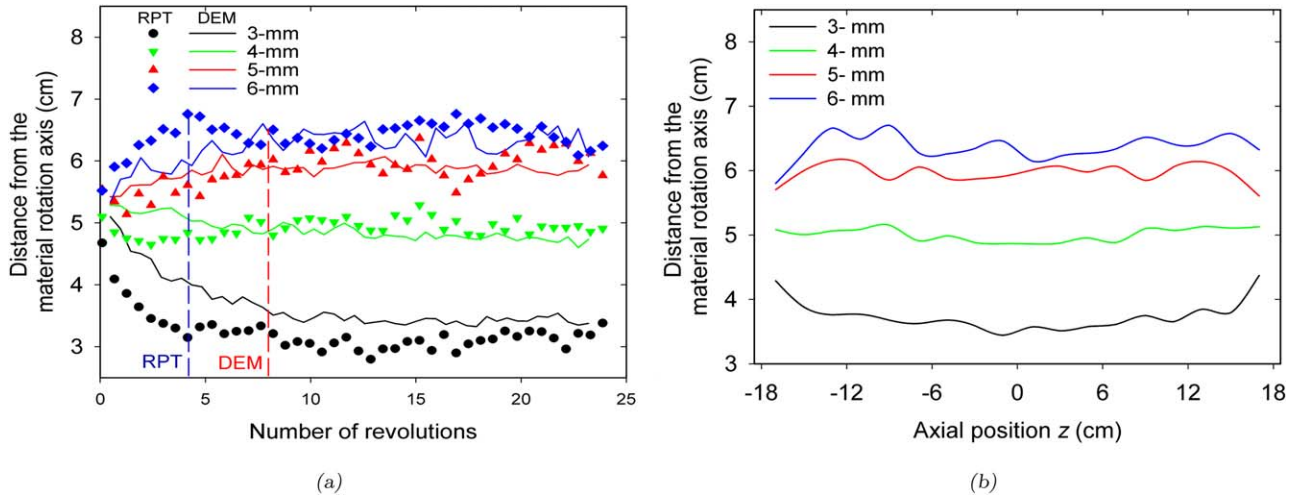

(a) (b)

Figure 7. (a) Time variation of $d^t(q)$, and (b) variation of $d^t(q)$ along the drum length for t =120 s (DEM results only).

[Color figure can be viewed in the online issue, which is available at wileyonlinelibrary.com.]

calculated. The progress of the axial segregation can be divided into three steps. In step I, the radial segregation develops and no significant axial segregation is observed. After 7 revolutions (~30 s), the radial segregation reaches a stable profile (as shown in Figures 5b, 7a) and the axial segregation continues (step II). After 60 s, the axial bands that are formed in steps I and II become richer in small or large particles (step III). There are two narrow bands near the end walls [Bands 1 and 5 when $|z| \in$ (0.15 m, 0.18 m)] and a wide band in the middle of the drum [Band 3 when $z \in$ (−0.1 m, 0.1 m)] where 5-mm and 6-mm particles accumulate. Two bands of small particles are formed between these three bands [Bands 2 and 4 when $|z| \in$ (0.10 m, 0.15 m)], which are concentrated in 3-mm and 4-mm particles.

Figure 9 shows the final concentration of the different-sized particles along the length of the drum after 120 s of DEM simulation. The red and blue solid lines show the initial concentrations of the 3 and 6-mm and 4 and 5-mm particles, respectively. As can be noticed, the concentration of the small 3 and 4-mm particles decreases near the end walls

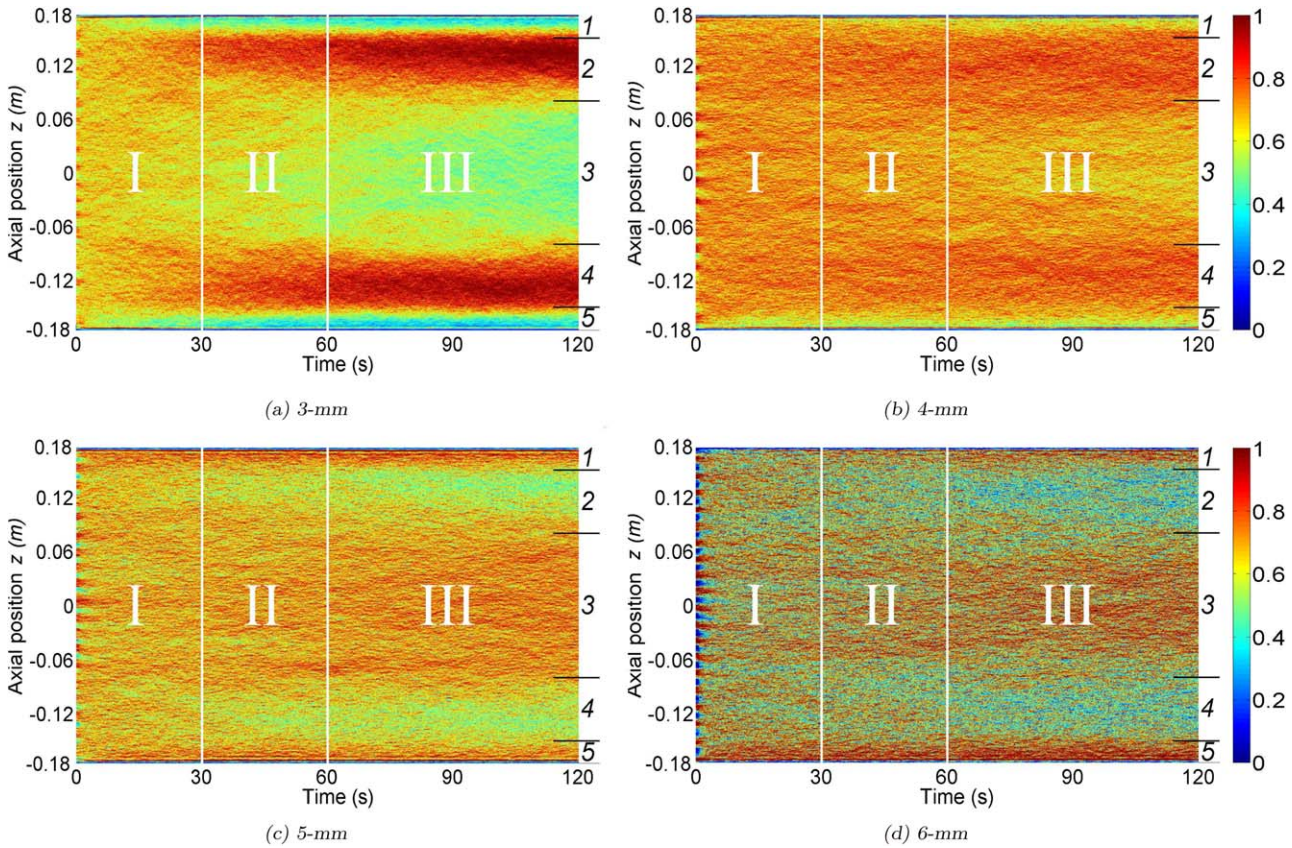

(a) 3-mm (b) 4-mm

(c) 5-mm (d) 6-mm

Figure 8. Axial segregation predicted by the DEM.

The colors show the probabilities of occurrence of corresponding particles. [Color figure can be viewed in the online issue, which is available at wileyonlinelibrary.com.]

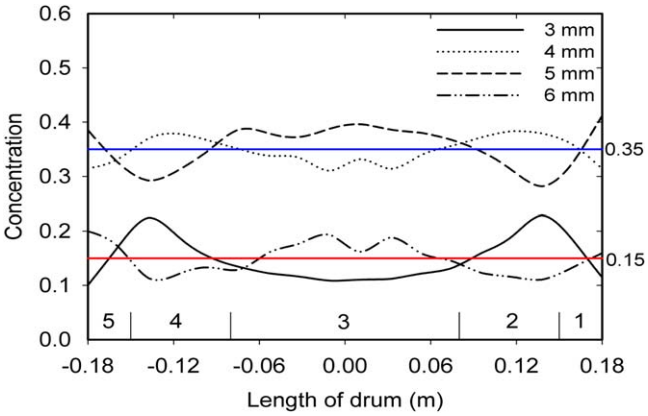

Figure 9. Concentration of the different-sized particles after 120 s of DEM simulation. See Table 1 for the overall concentration of each species.

[Color figure can be viewed in the online issue, which is available at wileyonlinelibrary.com.]

(Bands 1 and 5), whereas the concentration of the large 5 and 6-mm particles increases. This is in agreement with the reported data in the literature, which states that during the axial segregation of particles in a rotating drum, a band of large particles generally appears close to the end walls.[77] This can be explained by the end-wall effect as discussed earlier and explained by Chen et al.[78] Finally, in Bands 2 and 4, the concentration of the small and large particles increases and decreases, respectively.

Note that after 210 min (around 2500 revolutions) of RPT data acquisition, no significant axial segregation could be visualized from outside the drum, contrary to the DEM results. This difference can be explained by a larger friction coefficient used for the DEM simulations, thereby affecting the flow of particles near the end walls.

Quantification of axial dispersion

The DEM results may be utilized to quantify the dispersion of particles in the axial direction of the rotating drum.[79,80] It can also be measured using the trajectories of a single particle inside the granular bed.[3,5,13,16] The axial dispersion coefficient (D_{axial}) is related to the variance of the axial displacement distribution

$$D_{\text{axial}} = \frac{\sum_{i=1}^{N} \left(\Delta z_i - \overline{\Delta z}\right)^2 / \Delta t_i}{2N}. \tag{25}$$

For the DEM simulations and a simulation time of 120 s, Δz_i is the axial displacement of particle i in a full cycle, $\overline{\Delta z}$ the mean axial displacement, Δt_i the cycle time of particle i, and N the number of particles. A cycle corresponds to the travel of a particle along a closed streamline. For the RPT experiments, which lasted 210 min, the initial trajectory of the single tracer is split into a series of new trajectories, each of which can be associated to the flow of a different particle along a closed streamline representing a cycle. These trajectories have nonequal lengths that are a fraction of that of the initial trajectory. Therefore, Δz_i is the axial displacement along trajectory i (i =1,…, N), $\overline{\Delta z}$ the mean axial displacement, Δt_i the cycle time of trajectory i, and N the number of trajectories. It should be noted that in such a chaotic system, the streamlines are not perfectly close. Therefore, to calculate the axial dispersion coefficient, a streamline was considered closed when the y-component of the displacement of a given particle, when it gets back to the vicinity of its starting point along this streamline, was less than 0.5 cm.

Figure 10 displays the variations of D_{axial} in the active layer for the polydisperse system along a line perpendicular to the free surface at $x = 0$. As can be observed, the value of D_{axial} is of the order of 10^{-5}m^2/s, which indicates that the axial motion of the particles is slow and the tumbling drum suffers from weak axial mixing. These values are comparable with those reported in the literature. For instance, Ding et al.[69] obtained an axial dispersion coefficient of 3×10^{-6}m^2/s for 3-mm glass beads and a drum rotational speed of 9.6 RPM, whereas Sheritt et al.[16] reported values of the order of 10^{-5}m^2/s for rotational speeds of 5–25 RPM. Here, one may notice that D_{axial} is nearly constant along the y-direction although it increases near the free surface. This can be attributed to the fact that the closer the particles are to the free surface, the more freedom to move they have. The simulated results follow the same trends as the experimental measurements, yet the values predicted by the DEM are smaller than those obtained from the RPT. More precisely, the average value obtained from the RPT experiments is 1.54×10^{-5}m^2/s, as opposed 0.52×10^{-5}m^2/s with the DEM. This difference is due to the experimental error when tracking down the radioactive tracer in the drum and to the numerical error inherent to the DEM-based model. The impact of the particle properties used in the model is studied next.

Analysis of the DEM-based model

As it was shown in previous sections, there are discrepancies between the DEM and RPT results as regards axial dispersion and particle segregation in the drum. However, there is a good agreement in terms of the velocity profiles and the residence times of the granules, despite the use in the DEM simulations of smaller and higher values for the Young's modulus and the friction coefficients, respectively, in comparison with the measured values (Table 2). In the literature, a common practice often dodged by researchers is to set the value of several parameters such that results fit experimental data. In this section, an analysis of the DEM-based model is provided with respect to the granules properties, to identify

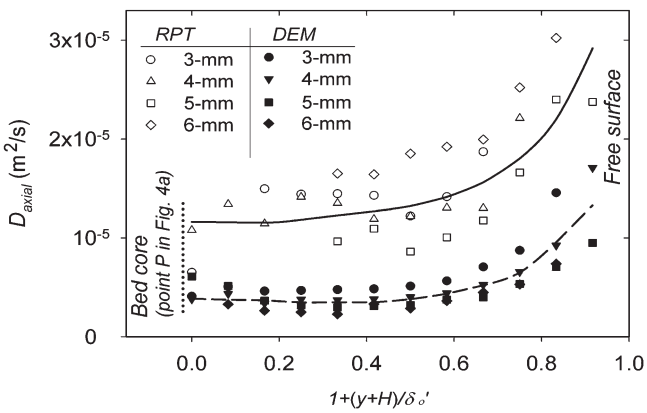

Figure 10. Axial dispersion coefficients determined from the displacements of the different-sized particles along a line perpendicular to the free surface at $x = 0$.

the most critical parameters and demonstrate how some parameters should be set to yield acceptable results when the value of one specific parameter is erroneous (e.g., Young's modulus).

As aforementioned, smaller values of the Young's modulus are generally chosen to avoid too large computational times. However, decreasing the value of the Young's modulus affects the contact force (see Eqs. 4–7). Therefore, it is of interest to investigate how the motion equation is affected when a smaller Young's modulus is used. In the case of particles with the same properties, the normal component of this equation for a binary collision, when gravity is taken into account, can be written as

$$m\frac{d\dot{\xi}_n}{dt}=k_n\xi_n^{\alpha}+S_n\xi_n^{\beta}\dot{\xi}_n-mg_n. \tag{26}$$

Following along the lines of Doucet,[81] dimensionless variables are next introduced

$$\hat{\xi}_n=\frac{\xi_n}{\xi_{n,m}}, 0<|\hat{\xi}_n|<1, \tag{27}$$

$$\hat{v}_n=\frac{\dot{\xi}_n}{v_{no}}, \begin{cases} 0<|\hat{v}_n|<1, \text{loading}, \\ 0<|\hat{v}_n|<CoR_n, \text{unloading}, \end{cases} \tag{28}$$

$$\hat{t}=\frac{v_{no}}{\xi_{n,m}}t, \tag{29}$$

where v_{no} is the initial normal impact velocity and $\xi_{n,m}$ is the maximum normal overlap during a collision. The value of $\xi_{n,m}$ can be obtained through Eq. 26 when $\dot{\xi}_n=0$. However, because of its complexity, this equation cannot be solved analytically. Neglecting the damping and gravity terms in Eq. 26, and using the normal contact forces given by Eqs. 4 and 5 provide a relationship between the maximum normal overlap and the Young's modulus through the conservation of mechanical energy

$$\frac{1}{2}mv_{no}^2=\frac{2}{5}k_n\xi_{n,m}^{\frac{5}{2}}. \tag{30}$$

Therefore

$$\xi_{n,m}=\left[\frac{15}{2\sqrt{8}}\frac{m(1-\nu^2)^2v_{no}^2}{E\sqrt{R}}\right]^{0.4}. \tag{31}$$

When the damping force cannot be neglected, DEM simulations have showed that for different values of the damping constant ($s_n=0.0$–0.2), a relationship similar to Eq. 31 is obtained over a wide range of values of the Young's modulus (20–68,900 MPa)

$$\xi_{n,m}\propto E^{-0.4}. \tag{32}$$

In particular, this implies that the elastic term is sufficient for many scaling situations. Substituting Eqs. 27–29 into Eq. 26 leads the following dimensionless motion equation

$$\frac{d\hat{v}_n}{d\hat{t}}+A_n\hat{\xi}_n^{\alpha}+B_n\hat{\xi}_n^{\beta}\hat{v}_n+C_n=0, \tag{33}$$

where

$$A_n=-\frac{3k_n\xi_{n,m}^{\alpha+1}}{4\pi\rho R^3v_{no}^2}, \tag{34}$$

$$B_n=-\frac{3S_n\xi_{n,m}^{\beta+1}}{4\pi\rho R^3v_{no}}, \tag{35}$$

$$C_n=\frac{\xi_{n,m}g_n}{v_{no}^2}. \tag{36}$$

C_n is the inverse of the Froude number based on the maximum overlap during the collision $(\xi_{n,m})$ and the initial impact velocity (v_{no}). This term is small with respect to the contact force term and can be neglected as a first analysis for many collisions occurring in the bed, where gravity is not the main driving force for granular flow. These dimensionless numbers can be used for a sensitivity analysis of the motion equation with respect to granule properties, and are valid for any contact force model (different k_n, S_n, α, and β). In particular, for the contact force model of this work, where $k_n=-\frac{4}{3}E^*\sqrt{R^*}$ and $S_n=-s_n\sqrt{6m^*E^*\sqrt{R^*}}$ from Eqs. 4 and 5, A_n and B_n become

$$A_n=\frac{1}{\rho\pi\sqrt{8}}\frac{E}{R^{2.5}v_{no}^2}\frac{\xi_{n,m}^{\alpha+1}}{(1-\nu^2)}, \tag{37}$$

$$B_n=s_n\left(\frac{9}{2}A_n\right)^{\frac{1}{2}}\xi_{n,m}^{\beta-\frac{1}{2}(\alpha-1)}. \tag{38}$$

Moreover, for $\alpha=\frac{3}{2}$ and $\beta=\frac{1}{4}$ (the exponents in the current contact force models), it can be noticed from Eq. 32 that dimensionless numbers A_n and B_n are independent of the Young's modulus. In such a case, the dimensionless equation of motion is then independent of the Young's modulus.

Such dimensionless numbers (A_n, B_n, and C_n) make it easier to investigate the effect of different parameters on particle motion. In particular, as the gravity term C_n can be neglected here, it is interesting to look at the ratio of A_n over B_n, which for the contact force models used in this work gives

$$\frac{A_n}{B_n}=\frac{1}{s_n}\left[\frac{9}{\rho\pi\sqrt{32}}\frac{E}{v_{no}^2(1-\nu^2)}\left(\frac{\xi_{n,m}}{R}\right)^{2.5}\right]^{\frac{1}{2}}. \tag{39}$$

In particular, straightforward calculations and the use of Eq. 31 show that, for a given impact velocity, a change in the Poisson's ratio of glass beads from 0.24 (see Table 2) to 0.30 (a common value in the literature) leads to a constant value of $\frac{A_n}{B_n}$. This means that the Poisson's ratio does not have an impact on the simulation results. As for the damping coefficient, glass beads have a high-energy restitution so that B_n has a smaller effect than A_n on the motion equation. A small variation of s_n then does not lead to a significant change in $\frac{A_n}{B_n}$. However, a large variation of s_n may result in a significantly different flow behavior. Indeed, it can be noticed by comparing Figures 11a and 7a (resp. Figures 11b and 7b) that increasing the damping coefficient (from 0.0075 to 0.3 for s_n, from 0.02 to 0.3 for s_t, from 0.065 to 0.3 for $s_{n,w}$, and from 0.02 to 0.3 for $s_{t,w}$) results in faster (resp. enhanced, near the end walls) radial segregation.

A similar analysis can be made for the tangential equation of motion by considering $\hat{\xi}_t=\frac{\xi_t}{\xi_{t,m}}$, $\hat{v}_t=\frac{\dot{\xi}_t}{v_{to}}$, and $\hat{t}=\frac{v_{no}}{\xi_{t,m}}t$

$$\frac{d\hat{v}_t}{d\hat{t}}+A_t\left[1-\left(1-\hat{\xi}_t\right)^{\frac{3}{2}}\right]+B_t\left(1-\hat{\xi}_t\right)^{\frac{1}{4}}\hat{v}_t+C_t=0, \tag{40}$$

$$A_t=\frac{1}{\rho\pi4\sqrt{2}}\frac{\hat{\xi}_n^{\alpha+1}}{R^{\frac{5}{2}}v_{to}^2}\frac{2-\nu}{(1-\nu)^2(1+\nu)}E\mu_s^2\xi_{n,m}^{\alpha+1}, \tag{41}$$

$$B_t=s_t\sqrt{6A_t}, \tag{42}$$

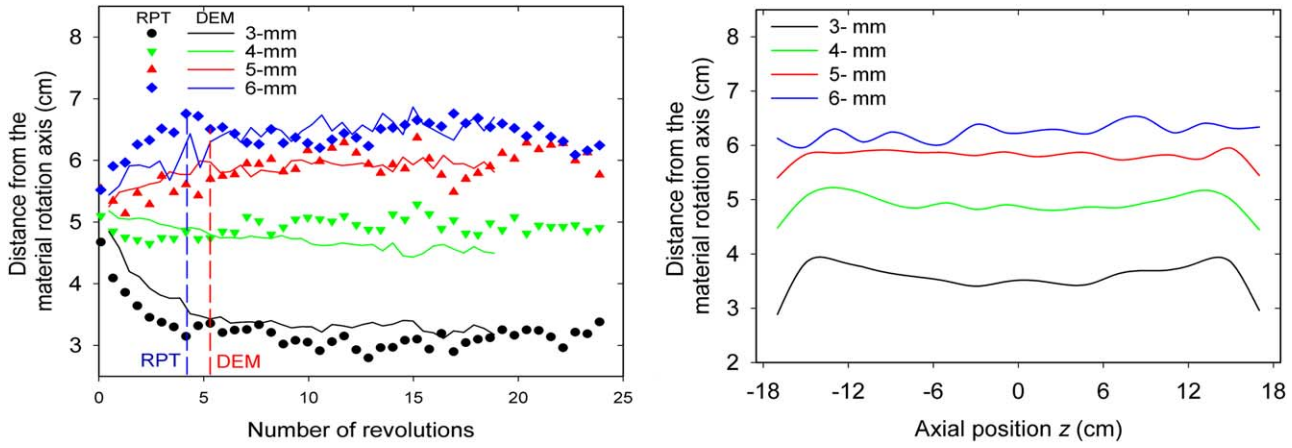

Figure 11. Effect of the damping constant ($s_n = 0.3$; $s_t = 0.3$; $s_{n,w} = 0.3$ and $s_{t,w} = 0.3$) on the (a) time variation of $d^t(q)$, and (b) variation of $d^t(q)$ along the drum length for $t = 100$s (DEM results only).

[Color figure can be viewed in the online issue, which is available at wileyonlinelibrary.com.]

$$C_t = \frac{2-\nu}{2(1-\nu)} \frac{\hat{\xi}_n}{v_{to}^2} g_t \mu_s \xi_{n,m}. \tag{43}$$

As C_n in the normal equation of motion, the term C_t can be neglected in Eq. 40 for many collisions in the granular bed, where gravity is not the governing force. Therefore, a discussion similar to that for $\frac{A_n}{B_n}$ can be made for $\frac{A_t}{B_t}$. In addition, varying the exponent in F_{el}^t (1 instead of $\frac{3}{2}$ in term $f_1(\xi_t)$ of Eq. 6) leads to insignificant differences in the predicted mixing behavior. This is mainly due to the relatively small role of the dissipative force in the equation of motion. Looking at $\xi_{n,m}$ in Eq. 32, it is also straightforward to realize that both A_t and B_t are independent of the Young's modulus when $\alpha = \frac{3}{2}$ and $\beta = \frac{1}{4}$. In such a case, the tangential motion of two colliding objects is not affected by the Young's modulus. In particular, these properties signify that the CoR in both the normal and tangential directions can be predicted correctly with the corresponding DEM-based models even if wrong values of the Young's modulus are used. More generally, it means that any value of the Young's modulus can be used without the need to adjust other parameters to compensate for the use of an erroneous value. This explains why the use of a much smaller Young's modulus and close to real values of the particle/particle friction coefficients may yield acceptable granular flow results. Of course, in practice, gravity does play a non-negligible role for many collisions, which is one reason why minor discrepancies are observed in the active layer of the bed with respect to the RPT data (Figure 1c). However, this does not suggest that if the values of the Young's modulus were matched, the results would also match perfectly. Indeed, there are other sources of errors in the DEM-based model, in particular the contact force model itself.

It is also worthwhile mentioning that C_t cannot be neglected in the wall region. In this case, one expects the tangential contact forces to be strong enough to overcome the gravity force acting on the particles and thus create a solid body motion in the passive layer. Otherwise, the particles close to the drum wall would slide, thereby changing the flow regime from rolling to slipping. Because the particles and the drum wall have very small relative tangential velocities, the effect of the dissipative force in Eq. 40 is negligible so that B_t does not play a significant role. Therefore, the values of the physical parameters appearing in A_t should be chosen such that the ratio $\frac{A_t}{C_t}$ is the same as that obtained with real values

$$\frac{A_t}{C_t} = K' E \mu_{w,s} \xi_{n,m}^{\alpha}, \tag{44}$$

where K' is independent of E and $\mu_{w,s}$. According to Eq. 32, $\xi_{n,m} \propto E^{-0.4}$ so that for our Hertzian force model $\left(\alpha = \frac{3}{2}\right)$

$$\frac{A_t}{C_t} = K \mu_{w,s} E^{0.4}, \tag{45}$$

where K includes a proportionality constant. The above equation can be applied as a criterion to choose $\mu_{w,s}$ when a smaller value of the Young's modulus is used in the DEM-based model to avoid too large computational time. This also explains why researchers have reported adequate simulation results despite the use of larger than real friction coefficients and smaller than real Young's modulus (see Table 3).

Considering the glass beads properties ($E = 68.9$ GPa and $\mu_{w,s} = 0.208$ from Table 2) and the value of the Young's modulus for the current DEM simulations ($E = 200$ MPa), Eq. 45 gives $\mu_{w,s} = 2.15$. This value is larger than the value used for the DEM simulations ($\mu_{w,s} = 0.45$ from Table 2). However, the DEM results are in good agreement with the RPT data as discussed in previous sections. In fact, $\mu_{w,s}$ from Eq. 45 respects the minimum value for the rolling regime, which corresponds to $Fr = 10^{-4}$ according to Mellmann.[1] For larger values of this Froude number, Fr = 0.018 in this study, the rolling regime may persist if, for instance, a smaller friction coefficient $\mu_{w,s}$ is used. Figure 12 shows the effect of the static friction coefficient $\mu_{w,s}$ on the simulation results of this work for varying values of the Young's modulus. The vertical axis corresponds to the average velocity of the particles in contact with the drum wall. As can be noticed, for small values of the Young's modulus, the use of a static friction coefficients larger than 0.35 guarantees that the velocity of these particles is close to 0.145 m/s, the rotational speed of the drum(ωR_D), which is the expected value for the particles flowing in the rolling regime. Therefore, as expected, even with a value of $\mu_{w,s}$ lower than what is predicted by Eq. 45, the rolling regime can be maintained at higher rotational speeds.

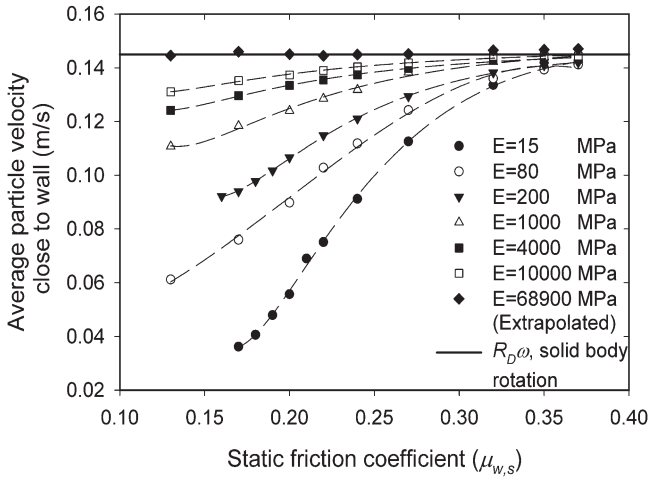

Figure 12. Effect of the friction coefficient $\mu_{w,s}$ on the simulation results when smaller values of the Young's modulus are used.

Figure 12 also teaches us that the larger the value of the Young's modulus, the less important the value of the friction coefficient$\mu_{w,s}$. Of course, in practice, the value chosen for $\mu_{w,s}$should guarantee that the resulting granular flow will be in the rolling regime. To examine the ability of the DEM-based model to correctly predict granular flow when the real value of the Young's modulus is used, the average particle velocities near the drum wall are displayed (◆ symbol) for such a case in the figure. Each point was obtained by extrapolating the least-square fitted results at smaller values of E and a specific friction coefficient. This extrapolated curve clearly shows that choosing the real value of E for a DEM simulation would generate particle velocities close to the wall that do not depend on $\mu_{w,s}$.

In summary, the findings of this work shed light on why a DEM simulation may lead acceptable results when smaller than real values of the Young's modulus are used. In fact, one might conclude that a DEM simulation could be conducted with extremely small values of the Young's modulus and a high friction coefficient for systems where gravity does not play a significant role. One should keep in mind that the analysis of the results of Figure 12 concerns the average particle velocity close to the drum wall. In practice, care should always be taken when using in a DEM simulation particle properties that are significantly different from measured ones.

Concluding Remarks

The objective of this work was to assess the accuracy of a DEM-based model and explain why good results can be obtained by the DEM even when nonreal values of particles properties are used. The validation was based on experimental RPT data on the mixing behavior and size segregation of a polydisperse mixture of glass beads in a rotating drum operated in rolling mode. All the properties of glass beads were measured experimentally or extracted from the literature and used in the DEM simulations except the Young's modulus and the friction coefficients, where smaller and higher values were applied, respectively. Both techniques (DEM and RPT) provide Lagrangian particle trajectories. A comparison of RPT and DEM results was performed based on the velocity profiles and residence times of the granules in the active and passive layers as well as their axial dispersion and mixing/segregation behavior. A good agreement was obtained in terms of the velocity profile and residence time. The DEM prediction for the axial dispersion along the radial direction was observed to comply with the RPT data, although with smaller axial dispersion coefficients. In the case of mixing and segregation, the DEM simulations predicted axial segregation, a phenomenon that was not observed in the experiments. This can be explained by the large friction coefficients used in these simulations.

An analysis of the DEM-based model was then performed with respect to the particle physical parameters. Dimensionless equations of motion were derived and analyzed in both the normal and tangential directions. They showed that when the gravity force on the particles can be neglected against the contact forces, the particle dynamics, and the dimensionless motion equations are not affected by the Young's modulus. In cases where the gravity force on the particles is non-negligible, a correlation was derived, which could be used to evaluate the sensitivity of simulation results to particle properties.

Finally, the findings reported in this work have shed light on the importance of the Young's modulus and the static friction coefficients on the particle dynamics. Future work will focus on the effect of these parameters on the force exerted by the particles on each other and the wall of the computational domain.

Acknowledgments

The financial contribution of Teva Canada, Praxair Inc. and the Natural Sciences and Engineering Research Council of Canada (NSERC) is gratefully acknowledged. All simulations were made possible thanks to the computational resources of Compute Canada. The authors are grateful to Majid Rasouli for helpful discussion on how to measure glass bead properties.

Notation

Abbreviations

DEM = discrete element method
CoR = coefficient of restitution
Fr = Froude number
LIF = light induced fluorescence
MPI = message passing interface
MRI = magnetic resonance imaging
NIR = near-infrared reflectance spectroscopy
PEPT = positron emission particle tracking
PIV = particle image velocimetry
PTV = particle tracking velocimetry
RPT = radioactive particle tracking
RSD = relative standard deviation

Roman symbols

A,B,C = dimensionless numbers for the motion equation
D_{axial} = axial dispersion coefficient, m^2/s
d = average distance of particles to point P
E = Young's modulus, Pa
$E^* = \left(\frac{1-\nu_i^2}{E_i^*} + \frac{1-\nu_j^2}{E_j^*}\right)^{-1}$ reduced Young's modulus of colliding particles, Pa
F = contact force, N
$f_1 = f_1 - \left(f_1 - \frac{\min\left(\xi_t, \xi_{t,m}\right)}{\xi_{t,m}}\right)^{3/2}$
$f_2 = \sqrt{1-|\xi_t|/\xi_{t,m}}$
G = particle shear modulus, Pa

g = gravitational acceleration, m/s^2
H = distance from the center of the drum to the free surface of material, m
K, K' = constants
k = stiffness coefficient
L = half-length of the free surface
l = particle position (x, y, z)
M = number of particle properties
m = particle mass, kg
$m^* = \left(\frac{1}{m_i^*} + \frac{1}{m_j^*}\right)^{-1}$: mean mass of colliding particles, kg
N = Number of particles in the drum
p = particle property
q = particle size
R = particle radius, m
$R^* = \left(\frac{1}{R_i^*} + \frac{1}{R_j^*}\right)^{-1}$: reduced radius of colliding particles, m
R_D = drum radius, m
$\overline{R}$ = average particle radius, m
r = particle radial position in the drum
S = damping coefficient
s = damping constant
t = time, s
$\hat{t}$ = dimensionless time
t_{act} = residence time in the active layer, s
t_{pas} = residence time in the passive layer, s
u_x = streamwise (x-direction) velocity, m/s
$u_{x,max}$ = maximum streamwise surface velocity, m/s
u_y = transverse (y-direction) velocity, m/s
$v_{p,f}$ = particle-fluid relative velocity, m/s
$\hat{v}$ = dimensionless particle relative velocity
v_o = particle initial impact velocity, m/s
x,y,z = position coordinates, m

Greek letters

α, β = exponents in the contact force models
γ, γ' = angle of streamline, rad
δ = thickness of the active layer, m
δ' = thickness of the active layer using the turning point criterion, m
$\varepsilon = 0.8766 + 0.163\ v$
η_{ws} = weak sense mixing index
η_{ss} = strong sense mixing index
θ = inclined surface angle
Λ = probability measure
μ = friction coefficient
μ_s = static friction coefficient
μ_r = rolling friction coefficient
ν = Poisson's ratio
ξ = particle overlap, m
$\hat{\xi}$ = dimensionless particle overlap
$\dot{\xi}$ = particle-particle (particle-wall) relative velocity, m/s
ρ = particle density, kg/m^3
τ_c = characteristic collision time, s
Ω = Rotational speed of the drum, RPM
ω = Rotational speed of the drum, rad/s

Subscripts and superscripts

* = reduced variable
dis = dissipative component of the contact force
el = elastic component of the contact force
i, j = colliding particles
m = maximum value of the particle overlap
n = normal direction of colliding particles
P = center of the granular bed
t = tangential direction of colliding particles
w = wall of the drum

Literature Cited

1. Mellmann J. The transverse motion of solids in rotating cylinders-forms of motion and transition behavior. *Powder Technol*. 2001; 118(3):251–270.
2. Henein H, Brimacombe J, Watkinson A. Experimental study of transverse bed motion in rotary kilns. *Metallur Trans B*. 1983;14(2): 191–205.
3. Ingram A, Seville J, Parker D, Fan X, Forster R. Axial and radial dispersion in rolling mode rotating drums. *Powder Technol*. 2005; 158(1–3):76–91.
4. Dury CM, Ristow GH, Moss JL, Nakagawa M. Boundary effects on the angle of repose in rotating cylinders. *Phys Rev E*. 1998;57(4): 4491–4497.
5. Alizadeh E, Dube O, Bertrand F, Chaouki J. Characterization of mixing and size segregation in a rotating drum by a particle tracking method. *AIChE J*. 2013;59(6):1894–1905.
6. Leonard G, Bertrand F, Chaouki J, Gosselin P. An experimental investigation of effusivity as an indicator of powder blend uniformity. *Powder Technol*. 2008;181(2):149–159.
7. Muzzio FJ, Goodridge CL, Alexander A, Arratia P, Yang H, Sudah O, Mergen G. Sampling and characterization of pharmaceutical powders and granular blends. *Int J Pharma*. 2003;250(1):51–64.
8. Jain N, Ottino J, Lueptow R. An experimental study of the flowing granular layer in a rotating tumbler. *Phys Fluids*. 2002;14(2):572–582.
9. Lueptow R, Akonur A, Shinbrot T. PIV for granular flows. *Exp Fluids*. 2000;28(2):183–186.
10. Nakagawa M, Altobelli S, Caprihan A, Fukushima E, Jeong EK. Non-invasive measurements of granular flows by magnetic resonance imaging. *Exp Fluids*. 1993;16(1):54–60.
11. Yamane K, Nakagawa M, Altobelli S, Tanaka T, Tsuji Y. Steady particulate flows in a horizontal rotating cylinder. *Phys Fluids*. 1998; 10(6):1419–1427.
12. Hawkesworth M, Parker D, Fowles P, Crilly J, Jefferies N, Jonkers G. Nonmedical applications of a positron camera. *Nucl Instrum Methods Phys Res Sect A*. 1991;A310(1–2):423–434.
13. Parker D, Dijkstra A, Martin T, Seville J. Positron emission particle tracking studies of spherical particle motion in rotating drums. *Chem Eng Sci*. 1997;52(13):2011–2022.
14. Lin J, Chen M, Chao B. A novel radioactive particle tracking facility for measurement of solids motion in gas fluidized beds. *AIChE J*. 1985;31(3):465–473.
15. Larachi F, Kennedy G, Chaouki J. A gamma ray detection system for 3-D particle tracking in multiphase reactors. *Nucl Instrum Methods Phys Res Sect A*. 1994;A338(2–3):568–576.
16. Sheritt RG, Chaouki J, Mehrotra AK, Behie LA. Axial dispersion in the three-dimensional mixing of particles in a rotating drum reactor. *Chem Eng Sci*. 2003;58(2):401–415.
17. Doucet J, Bertrand F, Chaouki J. An extended radioactive particle tracking method for systems with irregular moving boundaries. *Powder Technol*. 2008;181(2):195–204.
18. Khakhar D, Orpe AV, Ottino J. Continuum model of mixing and size segregation in a rotating cylinder: concentration-flow coupling and streak formation. *Powder Technol*. 2001;116(2–3):232–245.
19. Cundall P, Strack O. Discrete numerical model for granular assemblies. *Geotechnique*. 1979;29(1):47–65.
20. Sudah O, Arratia P, Alexander A, Muzzio F. Simulation and experiments of mixing and segregation in a tote blender. *AIChE J*. 2005; 51(3):836–844.
21. Lemieux M, Bertrand F, Chaouki J, Gosselin P. Comparative study of the mixing of free-flowing particles in a V-blender and a bin-blender. *Chem Eng Sci*. 2007;62(6):1783–1802.
22. Taberlet N, Newey M, Richard P, Losert W. On axial segregation in a tumbler: an experimental and numerical study. *J Stat Mech Theory Exp*. 2006;2006(07):1–17.
23. Moakher M, Shinbrot T, Muzzio FJ. Experimentally validated computations of flow, mixing and segregation of non-cohesive grains in 3D tumbling blenders. *Powder Technol*. 2000;109(1–3):58–71.
24. Iwasaki T, Satoh M, Koga T. Analysis of collision energy of bead media in a high-speed elliptical-rotor-type powder mixer using the discrete element method. *Powder Technol*. 2001;121(2-3):239–248.
25. Laurent B, Cleary P. Comparative study by PEPT and DEM for flow and mixing in a ploughshare mixer. *Powder Technol*. 2012;228:171–186.
26. Stewart RL, Bridgwater J, Zhou YC, Yu AB. Simulated and measured flow of granules in a bladed mixer-a detailed comparison. *Chem Eng Sci*. 2001;56(19):5457–5471.
27. Cantelaube F, Bideau D. Radial segregation in a 2D drum: an experimental analysis. *Europhys Lett*. 1995;30(3):133–138.
28. Dury CM, Ristow GH. Radial segregation in a two-dimensional rotating drum. *J Phys I*. 1997;7(5):737–745.

29. Ruelle D. A measure associated with Axiom A attractors. *Am J Math*. 1976;98:619–654.
30. Doucet J, Bertrand F, Chaouki J. A measure of mixing from Lagrangian tracking and its application to granular and fluid flow systems. *Chem Eng Res Des*. 2008;86(12):1313–1321.
31. Kruggel-Emden H, Simsek E, Rickelt S, Wirtz S, Scherer V. Review and extension of normal force models for the Discrete Element Method. *Powder Technol*. 2007;171(3):157–173.
32. Kruggel-Emden H, Wirtz S, Scherer V. A study on tangential force laws applicable to the discrete element method (DEM) for materials with viscoelastic or plastic behavior. *Chem Eng Sci*. 2008;63(6): 1523–1541.
33. Alizadeh E, Bertrand F, Chaouki J. Development of a granular normal contact force model based on a non-Newtonian liquid filled dashpot. *Powder Technol*. 2013;237:202–212.
34. Zhou Y, Xu B, Yu A, Zulli P. An experimental and numerical study of the angle of repose of coarse spheres. *Powder Technol*. 2002; 125(1):45–54.
35. Baxter J, Tuzun U, Burnell J, Heyes D. Granular dynamics simulations of two-dimensional heap formation. *Phys Rev E*. 1997;55(3-B): 3546–3546.
36. Tsuji Y, Tanaka T, Ishida T. Lagrangian numerical simulation of plug flow of cohesionless particles in a horizontal pipe. *Powder Technol*. 1992;71(3):239–250.
37. Li Y, Xu Y, Thornton C. A comparison of discrete element simulations and experiments for 'sandpiles' composed of spherical particles. *Powder Technol*. 2005;160(3):219–228.
38. Johnson K. Contact Mechanics. UK: Cambridge University Press, 1985.
39. Thornton C, Randall C. Applications of theoretical contact mechanics to solid particle system simulation. In: Satake M, Jenkins J, editors. Microme-chanics of Granular Materials, Elsevier Science, Amsterdam. Netherlands, 1988:133–142.
40. Bolz R, Tuve G. CRC Handbook of Tables for Applied Engineering Science. CRC Press, Boca Raton, 1970.
41. Foerster S, Louge M, Chang H, Allia K. Measurements of the collision properties of small spheres. *Phys Fluids*. 1994;6(3):1108–1115.
42. Amstock JS. Handbook of Glass in Construction. McGraw-Hill, 1997.
43. Zhou Y, Wright B, Yang R, Xu B, Yu A. Rolling friction in the dynamic simulation of sandpile formation. *Physica A*. 1999;269(2):536–553.
44. Bouffard J, Bertrand F, Chaouki J, Dumont H. Discrete element investigation of flow patterns and segregation in a spheronizer. *Comput Chem Eng*. 2013;49:170–182.
45. Balevicius R, Kacianauskas R, Mrz Z, Sielamowicz I. Discrete-particle investigation of friction effect in filling and unsteady/steady discharge in three-dimensional wedge-shaped hopper. *Powder Technol*. 2008;187(2):159–174.
46. Rowe R, Roberts R. 1—The mechanical properties of powders. In: Ganderton D, Jones T, McGinity J, editor. Advances in Pharmaceutical Sciences, Vol. 7, San Diego, CA: Academic Press, 1995, pp. 1–62.
47. Robinson BJ. Characterization of the viscoelastic behavior of pharmaceutical powders. Master thesis, Drexel University, Philadelphia, PA, 2009.
48. Lemieux M, Leonard G, Doucet J, Leclaire LA, Viens F, Chaouki J, Bertrand F. Large-scale numerical investigation of solids mixing in a V-blender using the discrete element method. *Powder Technol*. 2008;181(2):205–216.
49. Taberlet N, Losert W, Richard P. Understanding the dynamics of segregation bands of simulated granular material in a rotating drum. *Europhys Lett*. 2004;68(4):522–528.
50. Li D. 25—Friction and wear. In: Gale W, Totemeier T, editors. Smithells Metals Reference Book, 8th ed. Oxford: Butterworth-Heinemann, 2004, pp. 1–26.
51. Yang R, Zou R, Yu A. Microdynamic analysis of particle flow in a horizontal rotating drum. *Powder Technol*. 2003;130(13):138–146.
52. Yang R, Jayasundara C, Yu A, Curry D. DEM simulation of the flow of grinding media in IsaMill. *Miner Eng*. 2006;19(10):984–994.
53. Khodabakhshian R, Emadi B. Determination of the modulus of elasticity in agricultural seeds on the basis of elasticity theory. *Middle East J Sci Res*. 2011;7(3):367–373.
54. Sharan G, Lee JHA. Coefficient of friction of wheat grain on grain and steel. *Can Agric Eng*. 1970;12(1):14–17.
55. Schutyser M, Briels W, Rinzema A, Boom R. Numerical simulation and PEPT measurements of a 3D conical helical-blade mixer: a high potential solids mixer for solid-state fermentation. *Biotechnol Bioeng*. 2003;84(1):29–39.
56. Kaneko Y, Shiojima T, Horio M. Numerical analysis of particle mixing characteristics in a single helical ribbon agitator using DEM simulation. *Powder Technol*. 2000;108(1):55–64.
57. Zobel N, Eppinger T, Behrendt F, Kraume M. Influence of the wall structure on the void fraction distribution in packed beds. *Chem Eng Sci*. 2012;71:212–219.
58. Gonzalez-Montellano C, Ramirez A, Gallego E, Ayuga F. Validation and experimental calibration of 3D discrete element models for the simulation of the discharge flow in silos. *Chem Eng Sci*. 2011; 66(21):5116–5126.
59. Persson AS, Frenning G. An experimental evaluation of the accuracy to simulate granule bed compression using the discrete element method. *Powder Technol*. 2012;219:249–256.
60. Guo Y, Wassgren C, Ketterhagen W, Hancock B, Curtis J. Some computational considerations associated with discrete element modeling of cylindrical particles. *Powder Technol*. 2012;228:193–198.
61. Gonzalez-Montellano C, Ayuga F, Ooi J. Discrete element modelling of grain flow in a planar silo: influence of simulation parameters. *Granular Matter*. 2011;13(2):149–158.
62. Hartl J, Ooi JY. Experiments and simulations of direct shear tests: porosity, contact friction and bulk friction. *Granular Matter*. 2008; 10(4):263–271.
63. Kharaz A, Gorham D, Salman A. An experimental study of the elastic rebound of spheres. *Powder Technol*. 2001;120(3):281–291.
64. Mueth D, Jaeger H, Nagel S. Force distribution in a granular medium. *Phys Rev E*. 1998;57(3):3164–3169.
65. Ding Y, Seville J, Forster R, Parker D. Solids motion in rolling mode rotating drums operated at low to medium rotational speeds. *Chem Eng Sci*. 2001;56(5):1769–1780.
66. Weir G, Krouse D, McGavin P. The maximum thickness of upper shear layers of granular materials in rotating cylinders. *Chem Eng Sci*. 2005;60(7):2027–2035.
67. Liu XY, Specht E, Gonzalez O, Walzel P. Analytical solution for the rolling-mode granular motion in rotary kilns. *Chem Eng Process*. 2006;45(6):515–521.
68. Cheng NS, Zhou Q, Tan SK, Zhao K. Application of incomplete similarity theory for estimating maximum shear layer thickness of granular flows in rotating drums. *Chem Eng Sci*. 2011;66(12):2872–2878.
69. Ding Y, Forster R, Seville J, Parker D. Segregation of granular flow in the transverse plane of a rolling mode rotating drum. *Int J Multiphase Flow*. 2002;28(4):635–663.
70. Maneval J, Hill K, Smith B, Caprihan A, Fukushima E. Effects of end wall friction in rotating cylinder granular flow experiments. *Granular Matter*. 2005;7(4):199–202.
71. Dube O, Alizadeh E, Chaouki J, Bertrand F. Dynamics of nonspherical particles in a rotating drum. *Chem Eng Sci*. 2013;101:486–502.
72. Meier S, Lueptow R, Ottino J. A dynamical systems approach to mixing and segregation of granular materials in tumblers. *Adv Phys*. 2007;56(5–6):757–827.
73. Lacey P. Development in the theory of particle mixing. *J Appl Chem*. 1954;4:257–268.
74. Doucet J, Bertrand F, Chaouki J. Experimental characterization of the chaotic dynamics of cohesionless particles: application to a V-blender. *Granular Matter*. 2008;10(2):133–138.
75. Choo K, Molteno T, Morris S. Travelling granular segregation patterns in a long drum mixer. *Phys Rev Lett*. 1997;79(16):2975–2978.
76. Hill K, Kakalios J. Reversible axial segregation of rotating granular media. *Phys Rev E*. 1995;52(4):4393–4400.
77. Juarez G, Ottino J, Lueptow R. Axial band scaling for bidisperse mixtures in granular tumblers. *Phys Rev E*. 2008; 78(3):031306.
78. Chen P, Ottino JM, Lueptow RM. Onset mechanism for granular axial band formation in rotating tumblers. *Phys Rev Lett*. 2010; 104(18):188002.
79. Kohring G. Studies of diffusional mixing in rotating drums via computer simulations. *J Phys I*. 1995;5(12):1551–1561.
80. Third J, Scott D, Scott S. Axial dispersion of granular material in horizontal rotating cylinders. *Powder Technol*. 2010;203(3):510–517.
81. Doucet J. Mesure et caracterisation du melange dans les systemes granulaires denses. Ph.D. thesis, Polytechnique, Montreal, Canada (in French), 2008.

Manuscript received Dec. 4, 2012; and revision received Aug. 29, 2013.